Magnetically levitated spindle for long term testing of fiber reinforced plastic

Daniel Franz [a], Maximilian Schneider [a], Michael Richter [a], Stephan Rinderknecht [a]

[a] Institute for Mechatronic Systems in Mechanical Engineering, Technical University Darmstadt
Otto-Berndt-Straße 2, 64287 Darmstadt, Germany, franz@ims.tu-darmstadt.de

***Abstract*—This article describes a magnetically levitated spindle for long term cyclic fatigue strength testing of cylinders made of fiber reinforced plastic. These cylinders represent the outer-rotor of a kinetic energy storage. The realized spindle design has multiple eigenmodes below the operational speed range, which are described in the first part of this paper. Because the system is operated under vacuum conditions, the second part of this paper focuses on the heat generation and distribution on the rotor during operation. First, transient electromagnetic finite element simulations are described for the active magnetic bearings. These simulations are used to derive power losses of the active components on the rotor. Second, a finite element simulation characterizes the thermal behavior of the rotor and includes thermal radiation and conduction. Using the power losses calculated in the electromagnetic simulation, the thermal simulation provides the temperature of the rotor. Finally, these results are compared with measured data from the spindle. The comparison shows that the losses in the upper bearings are underestimated by the electromagnetic simulation. Nevertheless, the simulations show that the rotor overheats during long term operation, and thus further improvements on the control of the system have to be carried out.**

I. Introduction

Flywheels store electric energy as kinetic energy of the rotor and provide a possibility for short-term energy storage and load smoothening services. One flywheel design which is investigated, is an outer-rotor setup. It promises high energy densities due to the large radii of the rotor and high rotational speeds. The rotor is a magnetically levitated, hollow cylinder made out of carbon fiber reinforced plastic (FRP). All rotating components of the magnetic bearings and the electric machine are integrated on the inner circumference of the FRP rotor. One of the realized full scale systems is described in [1]. The energy density of the system increases with the radii of the rotor and its rotational speed, both leading to an increased stress in the FRP [2]. Consequently, high stress in the material accompanies a high energy density. Charging and discharging a flywheel leads to cyclically varying mechanical stresses. To investigate the cyclic stability and the lifetime of the FRP-rotor, cyclic material tests, such as cyclic transverse tensile tests [3], cyclic transverse compressive tests [4] and cyclic four-point bending tests are performed on material samples. These samples are thin walled and relatively easy to fabricate with high quality, whereas the rotor of the flywheel is much thicker and harder to produce in an industrial fiber winding process. Furthermore, thermal expansion of carbon fiber and the used epoxy plastic matrix differ, leading to inner stress when thick walled FRP-structures cool down from curing temperatures. This leads to a much higher probability of imperfections and defects in thick walled FRP-structures of an outer-rotor flywheel. Consequently, the applicability of the test with thin material samples on the rotor of the flywheel has to be investigated. It is not feasible to perform destructive investigation on a flywheel itself, because these systems are expensive and have high energy content, leading to a hazard of excessive damage. Hence, to examine the transferability of the results of material tests on an outer-rotor flywheel, a test rig is designed and build to perform cyclic tests on thick-walled FRP-cylinders.

A. Testing procedure

The state of stress in the test specimen should be as close as possible to the one in the flywheel. In the system described in [1] at its maximum speed of 15000 rpm the radial transverse compressive stress in the FRP is 60 MPa and the circumferential longitudinal stress is 389 MPa. To create a comparable state of stress in the test specimen a circumferentially segmented steel ring is placed inside the FRP-cylinder of the specimen, and rotated at 30000 rpm, which results in a radial transverse compressive stress of 100 MPa in the FRP. With an outer diameter of 190 mm, the surface speed of specimen reaches circa 298 m/s. The fatigue test consists of periodically reducing the speed to 15000 rpm, resulting in radial compressive stress of 26 MPa, and increasing it again to 30000 rpm. The circumferential longitudinal tension varies from 200 MPa to 775 MPa. Because of the well-known high tensile strength of carbon fiber, the chance of fiber fracture is low at this state of stress. The probability of matrix fracture is expected to be much higher (see [5]), but the compressive strength of the FRP is not well investigated yet.

It is planned to perform up to 200000 cycles per specimen. Due to the cycle time of 36 s, 200000 cycles will take about 83 days. An additional overload test is implemented, where the specimen is accelerated to 40000 rpm, resulting in a surface speed of nearly 398 m/s, a circumferential longitudinal tension of 1400 MPa and a radial compressive stress of 180 MPa. To reduce air drag and consequently the heating of the specimen, all tests are performed under vacuum conditions, with a pressure under 10^{-7} bar.

B. Test rig description

Figure 1 shows a section view of the designed test rig. A hub and a shaft coupling connect the specimen to the driving spindle. This configuration, rather than an outer-rotor setup, was chosen to protect the active parts in case of a failure of the specimen at high speeds. Each of the eight segments of the steel ring inside the FRP weighs 1.027 kg and the distance between

their center of gravity (CoG) and the rotation axis is about 55 mm. Hence, at 40000 rpm one segment contains around 30 kJ of kinetic energy. The surrounding containment is designed to absorb this energy in case of specimen failure. The design criteria for the containment were derived from [6]. The containment also serves as a vacuum chamber.

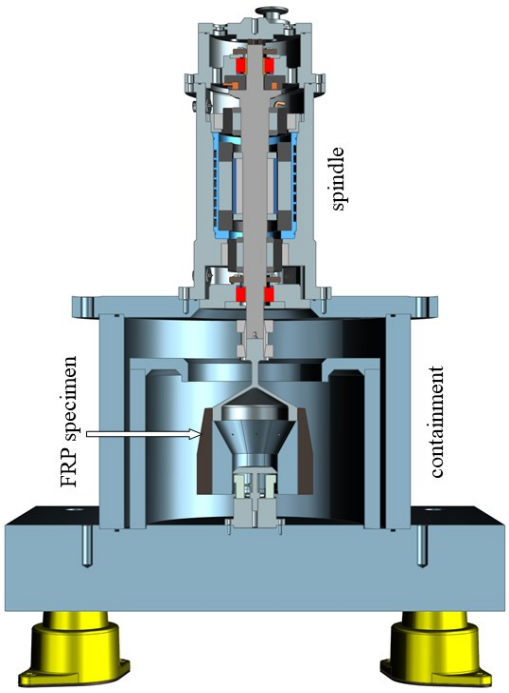

Figure 1. Cross section of the test rig

A detailed view of the spindle is shown in Figure 2. The motor in the middle is a water cooled permanent magnet synchronous machine (PMSM) with four poles, a maximum torque of 9.6 Nm and a maximum power of 30 kW.

In order to avoid excessive wear of the high-speed drive and heating of the specimen, the rotor is supported by active magnetic bearings (AMB). The radial AMB are designed in a heteropolar configuration with laminated cores on rotor and stator, both made out 0.2 mm thick sheets of non-oriented silicon steel. The radial position of the rotor is measured with eight eddy current sensors, two for each axis. To lift the combined mass of the spindle rotor and the specimen of around 20 kg, the axial AMB needs a large pole area, which leads to a big outer diameter of the thrust disk. Because of the high stress at high speeds, a monolithic design was chosen (see [6]). As a trade-off between mechanical strength and magnetic properties the rotor is made out of X14CrMoS17, which has a tensile strength of 500 MPa and saturation flux of nearly 1.6 T. The stator of the axial AMB is fabricated of soft magnetic composite. The axial position is detected by an inductive sensor at the upper end of the rotor. Two-rowed hybrid spindle bearings with a static load rating of 20 kN are used as backup bearings.

The first part of this paper discusses the mechanical behavior of the rotor. The second part focuses on the heating of the rotor during operation. Transient electromagnetic finite element simulations are used to derive the power losses on the rotor of the active components. Using these power losses, a thermal simulation provides the temperature of the rotor. Finally, these results are compared with measured data from the spindle.

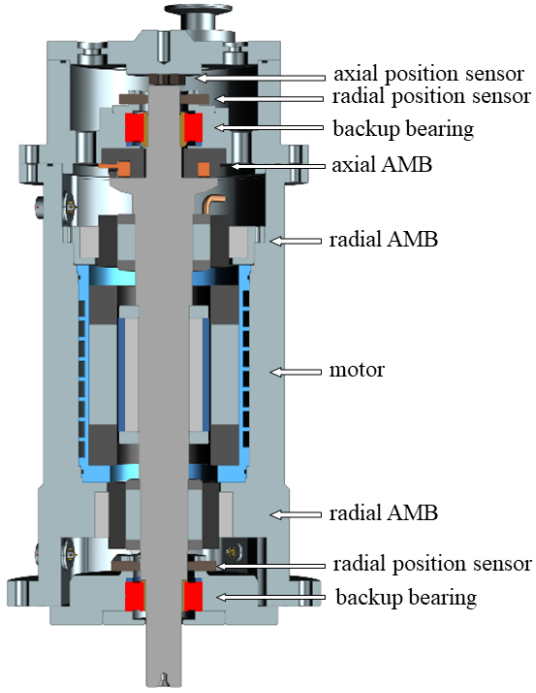

Figure 2. Cross section of the spindle

II. Rotor-dynamical Considerations

The moment of inertia of the specimen is about ten times higher than that of the rotor. The surface speed of the specimen is more than two times higher. To protect the rotor and the spindle when the specimen breaks, a defined breaking point is included in the hub (see Figure 3). This tapering also uncouples the dynamics of the rotor from the specimen to some extent.

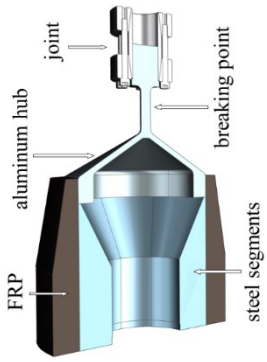

Figure 3. Cross section of the specimen

A. Calculations of the rotor eigenfrequencies

To predict the rotor behavior, a mechanical 3D-finite element (FE) model is created and evaluated. For modal analysis the AMB are modeled as springs with a constant stiffness of $2.5 \cdot 10^5$ N/m. Figure 4 shows the simulated Campbell-diagram of the rotor without the specimen. At 39 Hz and 86 Hz are the rigid body modes of the rotor in the AMB.

Both have to be crossed, when the rotor is accelerated. The first bending mode is at 1030 Hz, thus 353 Hz over the highest rotational frequency. The second bending mode is at 2170 Hz. Both split up in forward and backward mode.

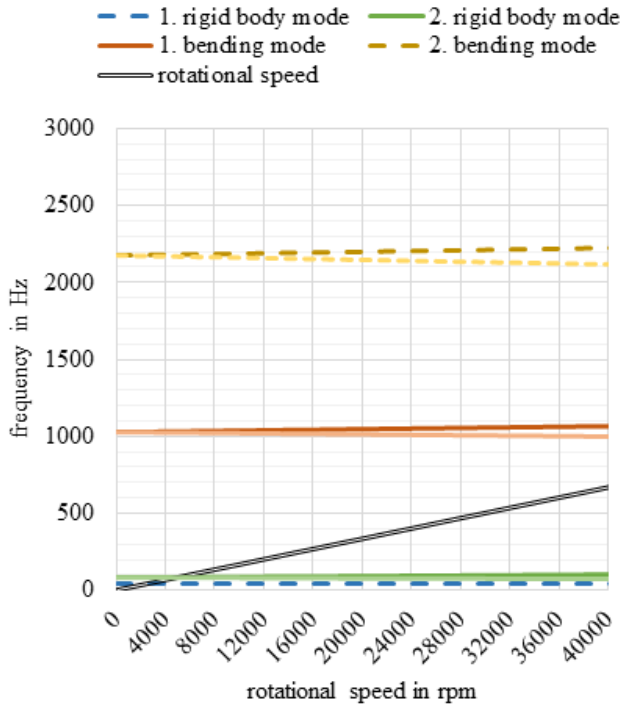

Figure 4. Campbell-diagram the rotor without the specimen

With the specimen, the first elastic mode is at 9 Hz, where the specimen tills at the tapering and the rotor stands still. At speeds higher than 9 Hz the specimen rotates around its CoG and there is no translational movement of its CoG in the higher eigenmodes. All bending eigenmodes of the rotor with the specimen under 1 kHz are shown in Figure 5. In the second, third and fourth mode the specimen is tilting around its CoG and in the fifth mode it does not move at all. The rotor shows elastic deformations beginning at the fourth mode. The nodes of the fifth mode are very close to the actuators and for the lower AMB even between actuator and sensor. Due to the high inertia ratio of the specimen the higher eigenfrequencies show a strong dependency on the rotational speed, which can be seen in the Campbell-diagram in Figure 6. For a clear presentation, only the forward modes are shown. The first three eigenfrequencies are below 15000 rpm, where the fatigue testing starts, and have to be passed before starting a test. The fourth eigenfrequency increases in such a way that it is not reached by speed-synchronous excitations within the operation range. However, due to the close proximity of the fourth mode the bandwidth of the AMB has to include this frequency. The fifth eigenfrequency has a minimum distance of 290 Hz to the rotational speed and thus it has to be filtered out from the position signal.

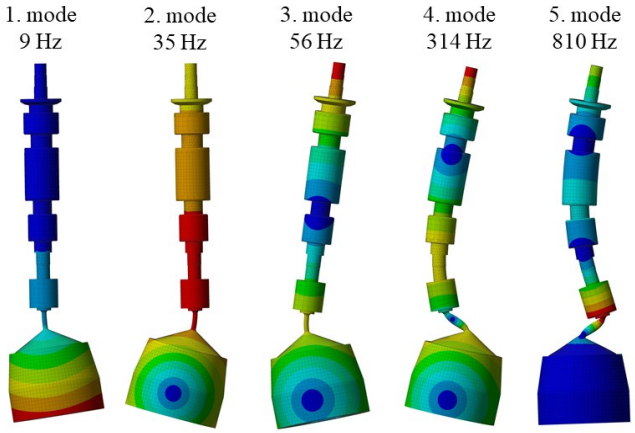

Figure 5. Bending eigenmodes below 1 kHz of the rotor with sample

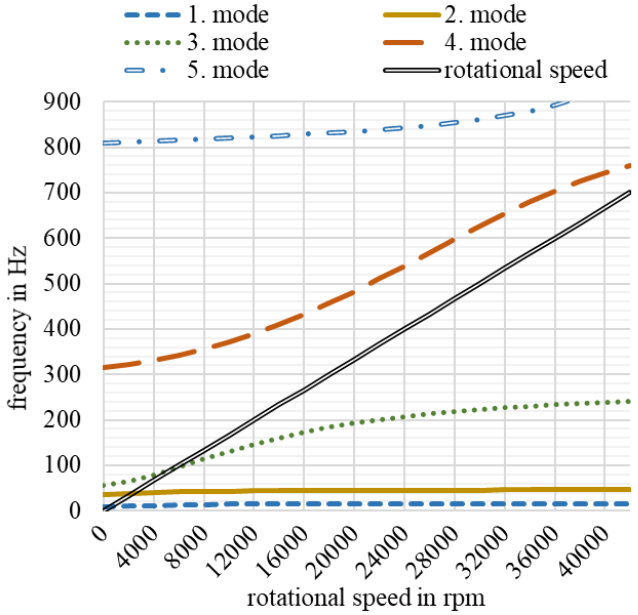

Figure 6. Campbell-diagram of forward modes of the rotor with the specimen

B. *Measured rotor eigenfrequencies*

A measured Campbell-diagram of the rotor without the specimen is shown in Figure 7. It is derived from the signals of the radial position sensors of the upper AMB, and thus the amplitude and frequency of the deflections over the rotational speed are shown. The highest deflections are synchronous to the rotational speed and its third harmonic. Odd harmonics of the rotational speed are clearly visible, whereas even harmonics are barely detectable.

The measured second bending mode is circa 100 Hz lower than the simulation predicted. Apart from this, the measured (Figure 7) and simulated (Figure 4) diagram show good resemblance.

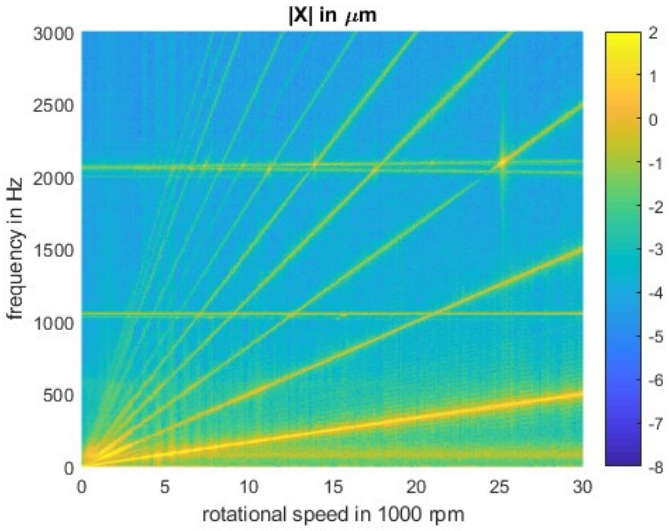

Figure 7. Measured Campbell-diagram of the rotor without specimen

These signals are measured parallel to the AMB and filtered with 4 kHz, therefore frequencies are visible which might be filtered out for the AMB control. This is the case for the first eigenfrequency of the rotor at 1057 Hz. It is filtered out of the signals for the AMB with a notch-filter, so there is no additional excitation of this eigenmode due to harmonics of the rotational speed. The second eigenfrequency at 2063 Hz is not filtered and hence peaks in the diagram can be seen when rotational harmonics hit the eigenfrequency. Every second odd harmonic excites the forward mode, whereas every other odd harmonic excites the backward mode. At 80 Hz is a rigid body tilting mode of the rotor in the AMB. It is visible because of the high distance of the upper radial AMB to its sensors and the use of a decentralized AMB-control.

III. Thermal Stability

The use of switching amplifiers for the PMSM and the AMB and the rotation leads to a change in the magnetic flux in the rotor and resulting iron losses. Without a medium for convection or thermal conduction through a physical contact, the rotor can only transfer heat to the stator via radiation. The calculation of power losses in the rotor and a thermal model will be discussed in the following passage. The temperature of the rotor is crucial for the feasibility of the cyclic fatigue testing, since the temperature of specimen affects the strength of the FRP.

A. Loss calculation of radial AMB

A quarter of the upper radial AMB is shown in Figure 8. The rotor is shown in the bottom left corner. The magnetic flux of the AMB is lead thru metal sheets, which surround the solid rotor. The nominal air gap between the rotor and the surrounding stator is 0.4 mm. The stator has eight poles. The implemented pole sequence is N-S-S-N-N-S-S-N. Flux leakage between two poles with equal flus direction, so N-N or S-S, is small, and thus two poles can be seen as one independent electromagnet. An idealized path of the magnetic flux ϕ in one magnet is shown in Figure 8. There are two coils on each pole, the inner for bias current I_B the outer for the control current I_Y. Both coils have the same number of turns, but thinner wire is used for the control coil. All bias coils are connected in series for one AMB and the control coils for each axis in one AMB.

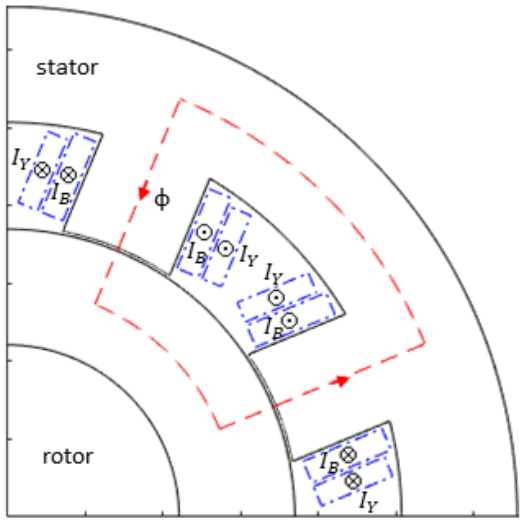

Figure 8. Quarter of the cross section of the upper radial AMB

The magnetic flux in a specific point of the rotor changes direction each time it passes a pole with a different flux direction, hence four times per revolution. This remagnetization leads to hysteresis losses P_h and excess losses P_e, as well as eddy currents and subsequent losses P_c. To calculate the losses a transient electromagnetic 2D-FE-model of the rotor is created and evaluated. Figure 9 shows the simulated magnetic flux density B in a quarter of the upper radial AMB at a rotational speed of 30000 rpm. The rotor turns clockwise. The currents are $I_B = 6$ A and $I_Y = 0$ A.

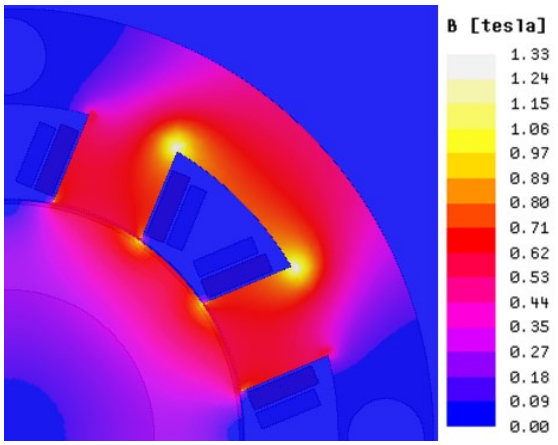

Figure 9. Magnetic flux density in the upper radial AMB

For the loss calculation the Bertotti formula (see [8]) in the form of (1) is applied, in which the three loss mechanisms are proportional to the product of different powers of the frequency f in which B changes and its amplitude B_m. The proportional factors are derived by fitting loss data to (1) for the used sheets, which yields:

$$k_c = 0.23\ \frac{\mathrm{Ws}^2}{\mathrm{T}^2\mathrm{m}^3},\ k_h = 193.6\ \frac{\mathrm{Ws}}{\mathrm{T}^2\mathrm{m}^3} \text{ and } k_e = 0\ \frac{\mathrm{Ws}^{1.5}}{\mathrm{T}^{1.5}\mathrm{m}^3}.$$

In this case there are no excess losses. The calculated losses for the upper and lower radial AMB are shown in Table 1.

$$P_{v,B} = P_c + P_h + P_e, \text{ with}$$
$$P_c = \int k_c (f B_m)^2 \, dV$$
$$P_h = \int k_h f B_m^2 \, dV \quad (1)$$
$$P_e = \int k_e (f B_m)^{1.5} \, dV$$

Table 1: Rotational losses in radial AMB

	15000 rpm	22000 rpm	30000 rpm
Upper AMB	8.2 W	15.6 W	26.0 W
Lower AMB	6.3 W	13.4 W	21.4 W

Additionally, the switching of the amplifiers leads to further high frequency changes in the magnetic flux. The resulting losses can be calculated with the same model and are 0.66 W for the upper AMB and 0.65 W for the lower AMB.

B. Loss calculation of axial AMB

Idealized the magnetic flux in the axial AMB is symmetric to the rotational axis, so no remagnetization losses should occur due to rotation. Nevertheless, in the solid thrust disk of the axial AMB the switching of the amplifier leads changes in the magnetic flux and consequently to rotor losses. Without the use of laminations or composites, eddy currents losses dominate and therefore, the other mechanisms are neglected. To calculate the losses a transient electromagnetic 2D-FE-modell is evaluated. Figure 10 shows the magnetic flux density B in the axial AMB with an air gap of 0.4 mm and a coil current of 3.15 A. The resulting force is 200 N. This force is required to lift the rotor with the specimen, with a total weight of 20.3 kg. The rotor alone weighs 8.6 kg. Without the specimen 84.4 N and 2 A are required.

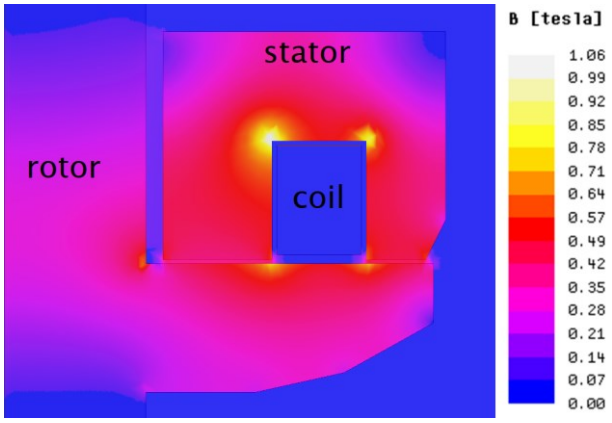

Figure 10. Magnetic flux density in the axial AMB

Changes of the magnetic flux in the rotor result in eddy currents and therefore in an nonzero current density J in the rotor. Eddy current losses $P_{v,J}$ are calculated as the integral of the square of J over the rotor volume V, divided by the conductivity of the rotor material σ_{el} (see eq. (2)). The conductivity of X14CrMoS17 is $\sigma_{el} = 1.43 \cdot 10^6 \frac{1}{\Omega m}$.

$$P_{v,J} = \frac{1}{\sigma_{el}} \int J^2 \, dV \quad (2)$$

Because eddy currents oppose their provoking field, high frequency changes of the magnetic field only affect the outer layers of the conducting material. Hence, eddy currents are also limited to a thin region on the surface of the rotor (see Figure 11). The losses of the axial AMB on the rotor derived by (2) due to the amplifier switching are under 0.1 W.

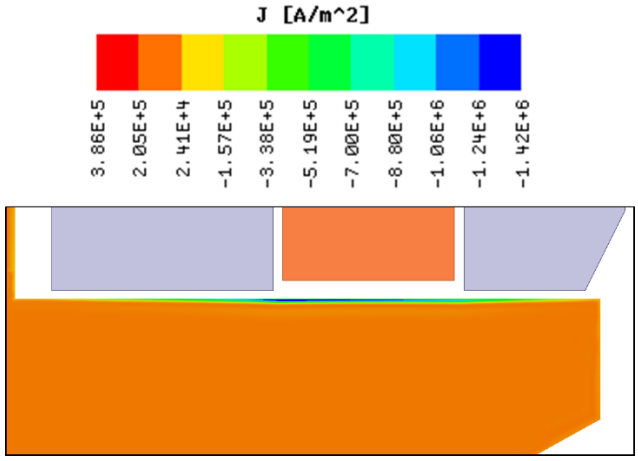

Figure 11. Current density in the surface area of the thrust disk during switching of the axial AMB

C. Loss calculation of the permanent magnet synchronous machine

The last component that induces losses on the rotor is the PMSM. Here the magnetic field rotates synchronously to the rotor. Remagnetization of the rotor occurs because of flux drops at slots in the stator and non-harmonic increase of the current, caused by the switching of the inverter. Again the losses are calculated via a transient electromagnetic 2D-FE model. The losses in the solid permanent magnets are calculated with eq. (2). Underneath the permanent magnets the rotor is laminated to reduce further harmonic losses. Remagnetization losses in the lamination are calculated according to eq. (1). The corresponding coefficients are:

$$k_c = 0.12 \, \frac{\mathrm{Ws}^2}{\mathrm{T}^2\mathrm{m}^3}, \; k_h = 166.7 \, \frac{\mathrm{Ws}}{\mathrm{T}^2\mathrm{m}^3} \text{ and } k_e = 3.24 \, \frac{\mathrm{Ws}^{1.5}}{\mathrm{T}^{1.5}\mathrm{m}^3}.$$

Results for different phase currents and rotational speeds are shown in Figure 12. The losses increase nearly linearly with the speed above 10000 rpm. For root mean square values of the phase current (rms) below 10 A_{rms}, losses are nearly independent of the phase current.

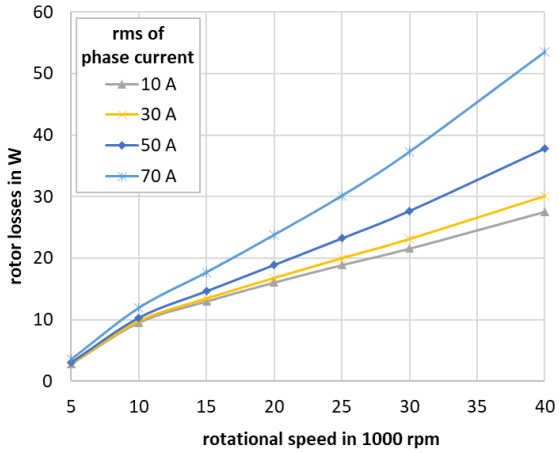

Figure 12. Rotor losses of the permanent magnet synchronous machine

D. *Simulation of thermal rotor behavior*

The simulation is performed using a 3D-FE-model of a quarter of the test rig. While the rotor transmits thermal energy to the stator via radiation, the stator radiates heat to the rotor as well. For real materials the coefficient of emission is smaller than one. This implies that only a part of the radiation which hits a surface is absorbed while the rest is reflected. Thus, when considering the heat exchange between two surfaces through radiation, both surfaces have to be taken into account. Consequently, for the simulation of the rotor heating, the inner surface of the stator has to be included in the model.[1] In the simulation it has to be defined for each surface on the rotor, which surfaces of the stator are reached by its heat radiation and vice versa. The rotor is painted with a special lacquer at the AMB and the PMSM. The coefficients of emission are assumed to be 0.9 for the painted and 0.3 for the unpainted, blank parts. Because of the water cooling, the stator temperature is assumed to be constantly 40 °C. To obtain the temperature distribution in the rotor, heat conduction in the rotor is also taken into account in the model, with a conductivity of 25 W/Km.

The steady state rotor temperature during the test cycles is calculated by applying the mean loss value per cycle for each actuator. The cycle starts at 15000 rpm, which is held for 3 s, after which the rotor is constantly accelerated for 15 s to 30000 rpm, which again is held for 3 s and finally the rotor is constantly decelerates for 15 s to 15000 rpm. The cycle and the speed dependent losses are illustrated in Figure 13. The mean values are derived by integrating the power loss over one cycle and dividing it by the total cycle time. The results are shown in Table 2.

Table 2: Mean of losses on the rotor during cycling

Upper AMB	PMSM (10 A_{rms})	PMSM (37 A_{rms})	Lower AMB
17.1 W	16 W	19,8 W	14.3 W

[1] Neglecting the reflection on the surface of the stator reduces the simulated maximum steady state temperature of the rotor without the specimen by circa 12 °C.

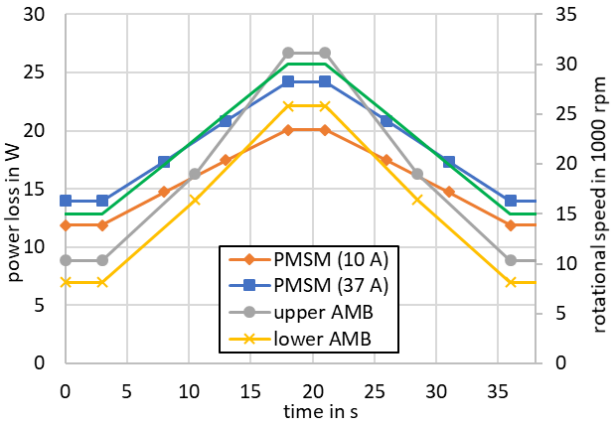

Figure 13. Rotational speed and losses during one cycle

The simulated temperature distribution in the center of the rotor over the axial length with and without the specimen is shown in Figure 14. In the specimen the temperature between the FRP and the steel segments is shown. Without the specimen the motor needs a phase current of about 3.7 A_{rms} to accelerate the rotor during the described cycle, but with the specimen about 37 A_{rms} is required. The losses of the PMSM are considered accordingly in the simulation. In both cases, the maximum temperature is around 150 °C with the highest temperatures at the upper AMB.

Even though higher rotor losses occur with the specimen, the temperature is lower than without it. This is because the large surface area of the FRP cylinder functions as a cooling element. The thin tapering at the hub leads to a large temperature drop, preventing the temperature of the FRP to from exceeding 52 °C. The normal operation temperature of the FRP in the flywheel is under 80 °C. But the magnets of the PMSM should not be used over 120 °C. Thus long term tests might only be feasible with cooling breaks, or by reducing rotor losses.

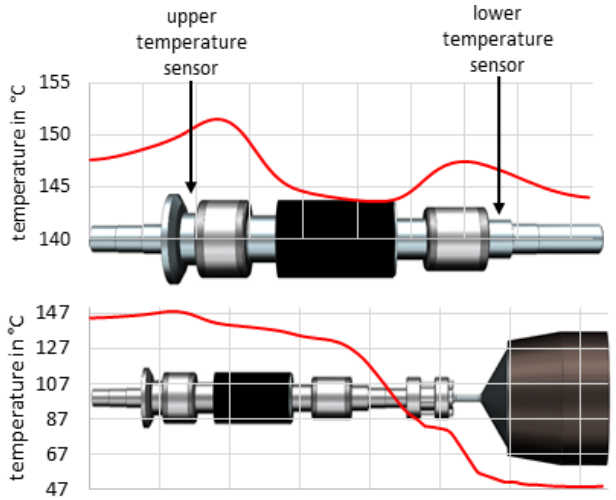

Figure 14. Temperature of the rotor with and without the specimen in the steady state

E. *Temperature messurements*

The rotor temperature is measured contactless with two infrared sensors: one between the upper radial AMB and the thrust disk and one next to the lower radial position sensors, below the lower AMB (see Figure 14). The utilized sensors can measure the temperature of metallic surfaces, but only above 50 °C. Figure 15 compares the measured temperatures on both positions with the simulations. While the rotor temperature of both positions is nearly the same in the simulation, it varies considerably in the measurement. The model underestimates the rotor heating at the upper temperature sensor, while simulation and measurement match relatively well for the lower sensor.

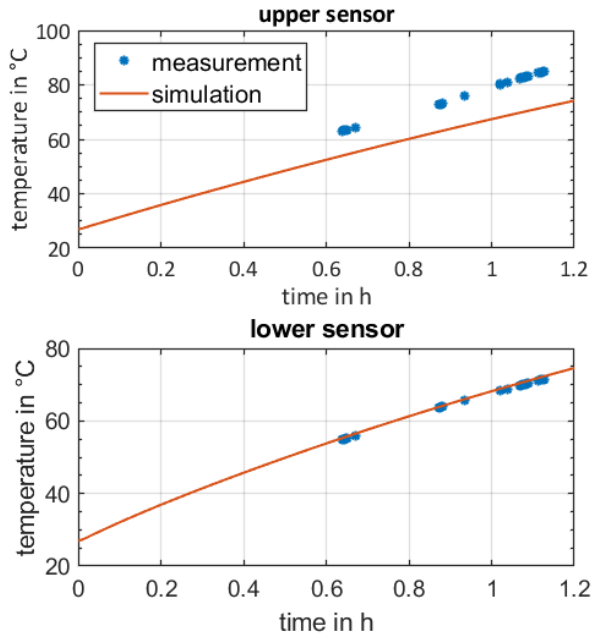

Figure 15. Simulated and measured rotor temperatures without the specimen

IV. Discussion

To match the simulated with the measured temperature at the upper sensor, about 6.8 W of additional losses in the upper radial or the axial AMB are required in the simulation (see Figure 15). The additional power leads to an increase of the maximum steady state temperature of the rotor without the specimen to 170 °C and with the specimen to 167 °C.

For the loss calculation it was assumed that the axial AMB is perfectly symmetric to the rotational axis. In reality small circumferential variations in the material of stator and rotor lead to flux changes during rotation and hence to higher rotor losses. Furthermore, control activities in the AMB are neglected in the simulation, but during the measurement, considerable movements in the axial direction were observed. Additionally, the upper radial AMB has to stabilize the 80 Hz tilting frequency, as seen in Figure 7. In the lower radial AMB this frequency is scarcely present, because its position sensors are much closer to the actuator.

When power losses in the upper AMB are increased in the thermal simulation, the temperature of the lower sensor will also rise (see Figure 15). This implies that either the losses in the lower AMB or the motor are overestimated or the thermal model is inaccurate. But additional power losses of 6.8 W in the thrust disk, lead to an increase in steady state temperature of the lower sensor of about 6 °C. So with adjusted loss calculation, the model seems suitable.

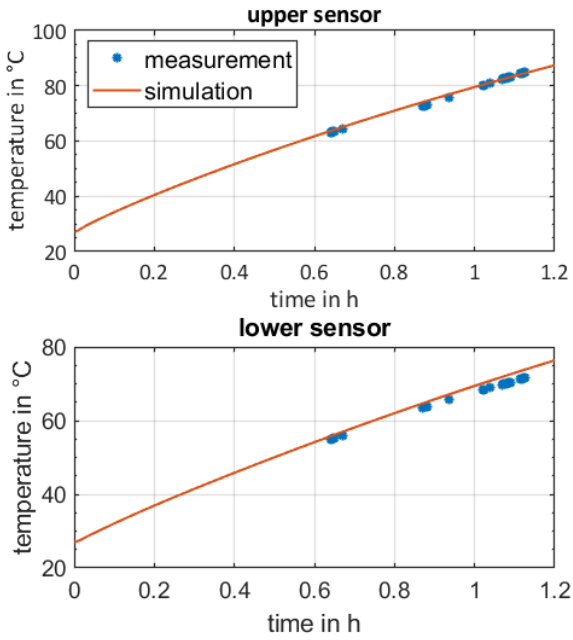

Figure 16. Simulated and measured rotor temperatures without the specimen with additional 6 W of power losses at the axial AMB in the simulation

For long term test without cooling interruptions, rotor losses have to be reduced. The highest simulated loses are rotational losses in the radial AMB and the PMSM. One way for loss reduction in the radial AMB, without major changes in the spindle hardware, is to reduce the bias current. While doing so, the controllability of the rotor has to be insured, particularly while passing low frequencies where many eigenfrequencies are present. The adjustment of the bias with the rotational speed might be necessary. Further loss reduction can be accomplished by reducing the control activity. A centralized control of the radial AMB should reduce the activities in the upper radial AMB. To realize a centralized control, however, the amplifiers need to be replaced. An overview of loss reduction strategies in AMB can be found in [9].

Acknowledgment

Supported by:

Federal Ministry
for Economic Affairs
and Energy

on the basis of a decision
by the German Bundestag

References

[1] L. Quurck, M. Richter, M. Schneider, D. Franz, S. Rinderknecht, "Design and practical realization of an innovative flywheel concept for industrial applications," *Proceedings of SIRM2017 – 12. Internationale Tagung Schwingungen in Rotierenden Maschinen*, pp. 151-160, 2017

[2] S.M. Arnold, A.F. Saleeb, N.R. Al-Zoubi, "Deformation and life analysis of composite flywheel disk systems" *Composites Part B: Engineering,* vol. 33, pp. 433–459, 2002

[3] ISO 527-5, "Plastics - Determination of tensile properties - Part 5: Test conditions for unidirectional fibre-reinforced plastic composites", 2009

[4] ISO 14126, "Fibre-reinforced plastic composites - Determination of compressive properties in the in-plane direction", 1999

[5] M. Knops, "Analysis of failure in fiber polymer laminates", vol. 2, Springer, Berlin, 2008

[6] A.C. Hagg, G.O. Sankey, "The Containment of Disk Bunt Fragments by Cylindrical Shells" ASME *Journal of Engineering for Power,* pp. 114-123*,* Detroit, 1974

[7] R. Larsonneur, "Design and control of active magnetic bearing systems for high speed rotation", Diss. ETH No. 9140, Zuerich, 1990

[8] G. Bertotti, "General properties of power losses in soft ferromagneticmaterials," *IEEE Transactions on magnetics*, vol. 24, no. 1, pp. 621-630, 1985

[9] S. Gaechter, H. Kameno, "Application of zero-bias current active magnetic bearings to flywheel energy storage systems", *Koyo Engineering Jurnal* , No 165E, 2004, pp. 25-30